7

# Application of Remote Sensing for Tsunami Disaster

Anawat Suppasri[1], Shunichi Koshimura[1], Masashi Matsuoka[2], Hideomi Gokon[1] and Daroonwan Kamthonkiat[3]
[1]*Tsunami Engineering Laboratory, Disaster Control Research Centre, Graduate School of Engineering, Tohoku University*
[2]*National Institute of Advanced Industrial Science and Technology*
[3]*Department of Geography, Faculty of Liberal Arts, Thammasat University*
[1,2]*Japan*
[3]*Thailand*

## 1. Introduction

This chapter aims to introduce an application of remote sensing to recent tsunami disasters. In the past, acquiring tsunami damage information was limited to only field surveys and/or using aerial photographs. In the last decade, remote sensing was applied in many tsunami researches, such as tsunami damage detection. Satellite remote sensing can help us survey tsunami damage in many ways. In general, the application of remote sensing for tsunami disasters can be classified into three stages depending on time and disaster-related information. In the first stage, general damage information, such as tsunami inundation limits, can be obtained promptly using an analysis combined with ground truth information in GIS. The tsunami inundation area is one of the most important types of information in the immediate aftermath of a tsunami because it helps estimate the scale of the tsunami's impact. Travel to a tsunami-affected area for field surveys takes a lot of time, given the presence of damaged roads and bridges, with much debris as obstacles. In the second stage, detailed damage interpretation can be analysed; i.e., classification of the building damage level. Recently, the quality of commercial satellite images has improved. These images help us clarify, i.e., whether a house was washed away or survived; they can even classify more damage levels. The third stage combines the damage and hazard information obtained from a numerical simulation, such as the tsunami inundation depth. The damage data are compiled with the tsunami hazard data via GIS. Finally, a tsunami vulnerability function can be developed. This function is a necessary tool for assessing future tsunami risk.

The contents of this chapter are arranged in three sections:

- Satellite image analysis for detecting tsunami-affected areas
- Tsunami damage level classification by visual interpretation and image analysis
- Development of a tsunami vulnerability function by applying a numerical model

## 2. General satellite image analysis for tsunami-affected areas

### 2.1 NDVI analysis using optical high-resolution satellite imagery

*Tsunami inundation limit*

Recent advances in remote sensing technologies have expanded the capabilities of detecting the spatial extent of tsunami-affected areas and damage to structures. The highest spatial resolution of optical imageries from commercial satellites is up to 60–70 centimetres (QuickBird owned by DigitalGlobe, Inc.) or 1 metre (IKONOS operated by GeoEye). Since the 2004 Sumatra-Andaman earthquake tsunami, these satellites have captured images of tsunami-affected areas, and the images have been used for disaster management activities, including emergency response and recovery. To detect the extent of a tsunami inundation zone, NDVI (Normalised Difference Vegetation Index) is the most common index obtained from the post-event imagery, focusing on the vegetation change due to the tsunami penetration on land. The NDVI is calculated from these individual measurements as follows:

$$NDVI = \frac{NIR - R}{NIR + R} \tag{1}$$

where $R$ and $NIR$ stand for the spectral reflectance or radiance in the visible (red) and near-infrared bands, respectively. Focusing on the existence of tsunami debris, 100 points were sampled to identify the NDVI threshold to classify the tsunami inundation zone. As shown in Fig. 1, the NDVI values are calculated within a range 0.34 ± 0.05. As a result, the extent of the tsunami inundation zone is determined by the supervised classification based on the NDVI threshold. As shown in Figure 2 (a), the QuickBird imagery clearly detects the vegetation change between pre- and post-tsunami. Tsunami debris can be seen along the edge of the tsunami inundation zone. Figure 2 (b) shows the result of the detection of the tsunami inundation zone by applying the threshold value of NDVI, and the result is consistent with the field survey.

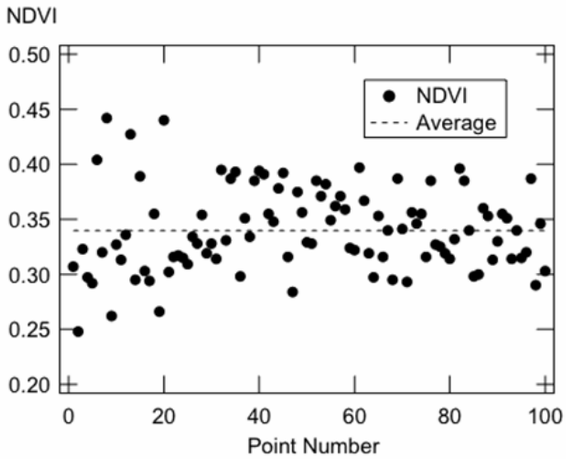


Fig. 1. Threshold value of NDVI within the tsunami inundation zone obtained from the analysis of the post-tsunami satellite imagery.

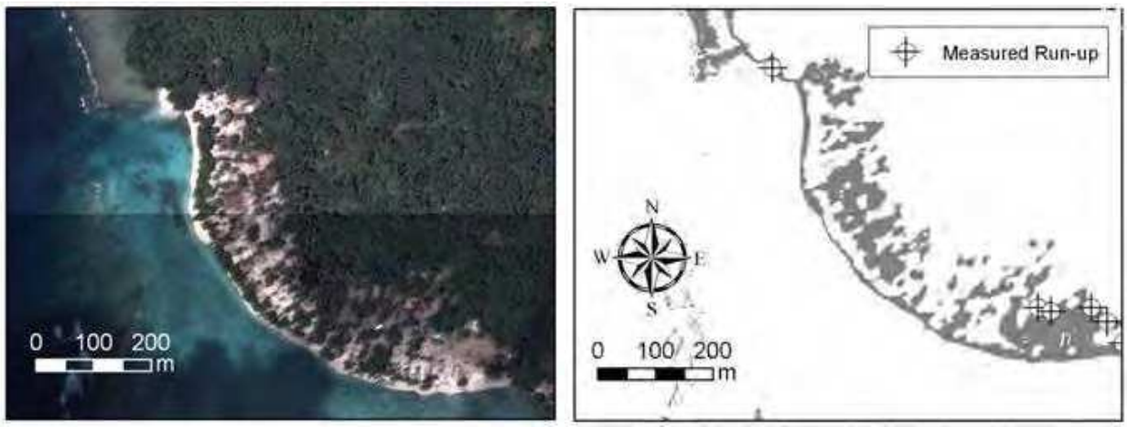


Fig. 2. (a) Vegetation change found from pre- and (b) post-event imageries and estimated extent of tsunami inundation zone by the supervised classification of NDVI.

*Damage and recovery monitoring of mangrove*

Because mitigation and protection against the 2004 Indian Ocean Tsunami was one of the important services that mangrove ecosystems provided in the affected areas, a six-year program to conserve and rehabilitate mangrove forests in the tsunami-impacted areas was implemented by the Thai Government after the tsunami. However, information on mangrove restoration and reforestation is limited to field surveys. Monitoring proposals were applied for a damaged mangrove area. Kamthonkiat et al. (2011) used ASTER images acquired in 2003, 2005 (two months after the 2004 Indian Ocean tsunami), 2006 and 2010 and the analysis using NDVI to monitor the mangrove recovery in tsunami-impacted areas in the southern part of Thailand. Figure 3 depicts the area of mangroves in 2003 in red and the area impacted by the tsunami in 2005 in dark blue and white for the same location. After the mangrove trees were uniformly or homogeneously replanted in the same location in the last quarter of 2005 in Takuapa District, the areas marked in red increased in 2006 and increased still further in 2010, as shown in Fig. 3 (*Note*: red represents vegetation or mangroves, white represents bare soil/sand, and blue/dark blue represent water). The recovery process can be detected, as some parts in light blue became red in 2006, and most became red in 2010 meaning the mangroves recovered to nearly the normal condition before the tsunami attack. These results show the abilities of geoinformatic technologies, especially regarding the time series analysis.

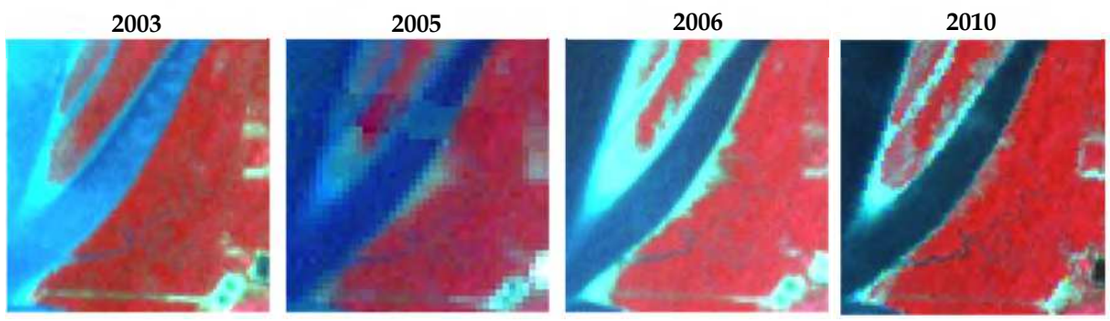


Fig. 3. Damage and recovery process due to the 2004 tsunami in Takuapa, Thailand

### 2.2 TerraSAR-X image analysis

Among the various sensors, SAR (Synthetic Aperture Radar) is remarkable for its ability to record the physical value of the Earth's surface (Henderson and Lewis, 1998). Unlike passive optical sensors, SAR enables the observation of surface conditions day or night, even through clouds. SAR interferometric analyses using phase information have successfully provided quantification of relative ground displacement levels due to natural disasters (Massonnet et al., 1993). More importantly, intensity information obtained from SAR represents a physical value (backscattering coefficient) that is strongly dependent on the roughness of the ground surface and the dielectric constant. Based on this idea, models for satellite C- and L-band SAR data were developed to detect building damage areas due to earthquakes by clarifying the relationship between the change in the backscattering coefficient from pre- and post-event SAR images (Matsuoka & Yamazaki, 2004; Matsuoka & Nojima, 2009) and then applying the models to tsunami-induced damage areas (Koshimura & Matsuoka, 2010). TerraSAR-X, which is the first German radar satellite with high-resolution X-band, was successfully launched on June 15, 2007, and has been in operation for data acquisition since early 2008. The day after the event, TerraSAR-X observed the coastal area in the affected regions by the StripMap-mode, which captures the Earth's surface with an approximately 3-metre resolution. Typically, man-made structures show comparatively high reflection due to the cardinal effect of structures and the ground. Open spaces or damaged buildings have comparatively low reflectance because they scatter the microwaves in different directions. Buildings may be reduced to debris by earthquake ground motion, and in some cases, the debris of buildings may be removed, leaving the ground exposed. Thus, the backscattering coefficient determined after building collapse is likely to be lower than that obtained prior to the event (Matsuoka & Yamazaki, 2004; Nojima et al., 2006). Inundated areas also show a lower backscattering coefficient because of the smooth surface and the dielectric constant of water bodies (Fig. 4 centre). By examining the backscattering characteristics of tsunami damage in typical areas, however, the reverse case occurred in some damaged areas in farmlands and controlled forests. To explain these anomalies in the post-tsunami TerraSAR-X image, several factors need to be considered, such as changes of the Earth's surface and its materials. Scattered debris from collapsed buildings, visible in the farmlands and bare ground in the post-tsunami image, show brighter reflections than in the pre-tsunami image (Fig. 4 centre).

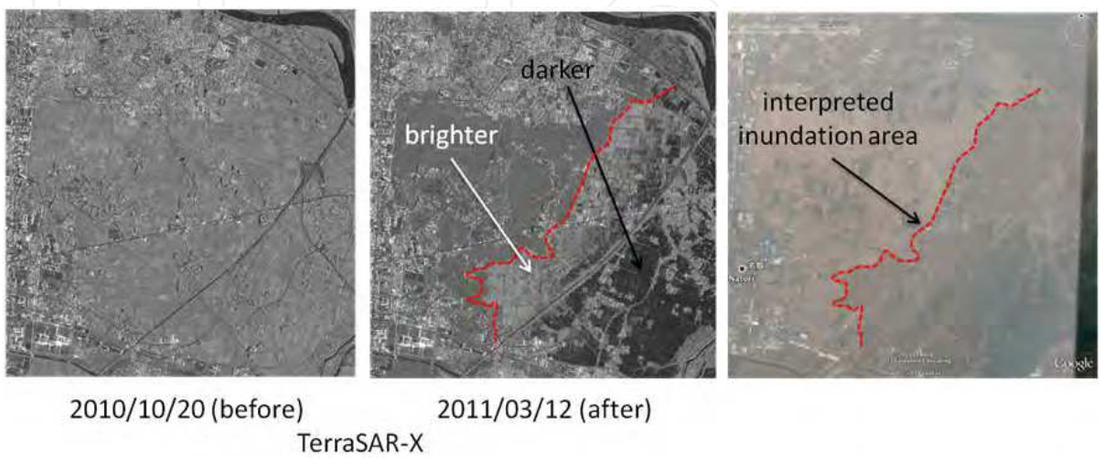


Fig. 4. Comparison between TerraSAR-X image and IKONOS (GeoEye) image

For the areas where some trees in the forest were washed away, the significant backscattering characteristics changed from volume scattering to surface scattering with significant roughness. These kinds of characteristics affecting the backscattering echo were identified in the tsunami-affected areas in the TerraSAR-X image. Following Nojima et al. (2006), the regression discriminant function for building damage was calculated from two characteristic values, the correlation coefficient and the difference in backscattering coefficient for pre- and post-event SAR images. First, following the accurate positioning of the two SAR images, a speckle noise filter with a 21×21 pixel window (Lee, 1980) was applied to each image. The difference value, $d$, is calculated by subtracting the average value of the backscattering coefficient within a 13×13 pixel window in the pre-event image from the post-event image (after – before). The correlation coefficient, $r$, is also calculated from the same 13×13 pixel window (Matsuoka & Yamazaki, 2004). The result of applying regression discriminant analysis, using the $d$ and $r$, is shown in Equation (2).

$$Z_{R1} = -A \cdot d - B \cdot r \tag{2}$$

Here, $Z_{R1}$ represents the discriminant score from the SAR images where the values of parameter A and B are 1.21 and 4.36, respectively. The pixels whose $Z_{R1}$ value is positive (red) are interpreted as suffering severe damage (Fig. 5 left). Because both coefficients are negative, higher and negative $d$ or smaller $r$ produce larger $Z_{R1}$ values. A preliminary formula for the C-band dataset was used because that for the X-band was unavailable. For this reason, the backscattered echoes were stronger in the post-tsunami image. To detect such damaged areas using image analysis, cases where the reverse occurs need to be considered. Therefore, the following Equation (3) was also calculated based on a positive value for the difference in backscattering coefficient $d$.

$$Z_{R2} = A \cdot d - B \cdot r \tag{3}$$

Here, $Z_{R2}$ represents another discriminant score where the values of parameters A and B are 1.21 and 4.36, respectively. Using this formula, the pixels whose $Z_{R2}$ value is positive (red) might be assigned as damaged areas (Fig. 5 centre).

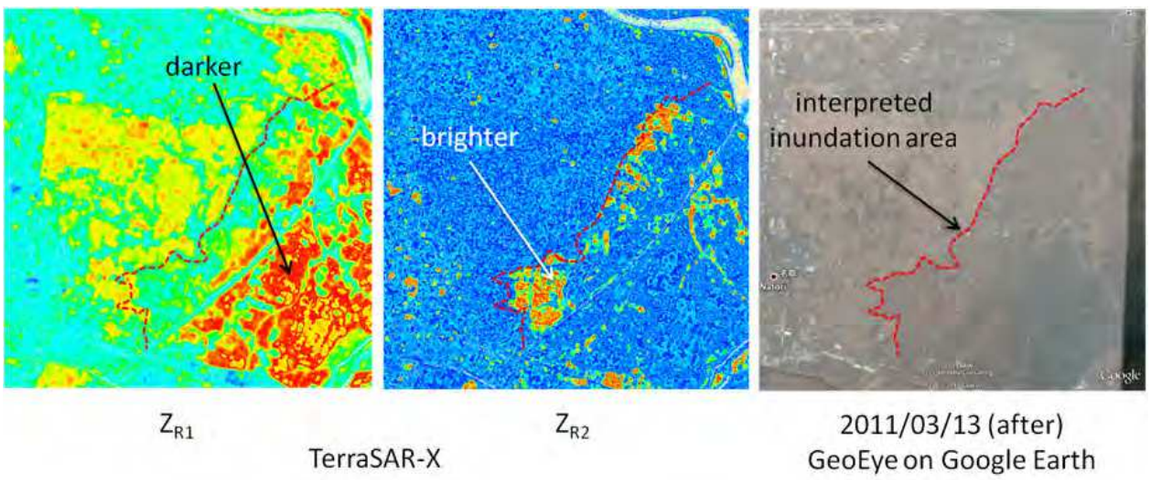


Fig. 5. Computed $Z_{R1}$ and $Z_{R2}$ from TerraSAR-X image to determine inundation area

Two discriminant scores, $Z_{R1}$ and $Z_{R2}$, were calculated for the TerraSAR-X image pair using the described procedure. The threshold values for $Z_{R1}$ and $Z_{R2}$ were determined to be 6 and 0, respectively. The extracted areas where the $Z_{R1}$ is larger than 6 or the $Z_{R2}$ is larger than 0 are shown in red in Fig. 6.

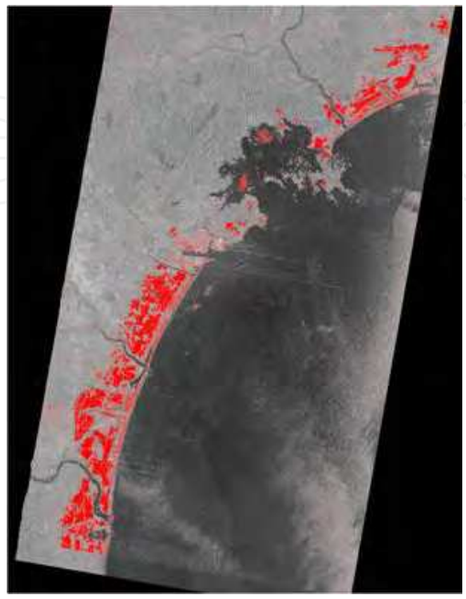

Fig. 6. Threshold values for $Z_{R1}$ and $Z_{R2}$ in the case of the 2011 Tohoku tsunami in Miyagi prefecture. The tsunami inundation area was extracted when the $Z_{R1}$ was larger than 6 or the $Z_{R2}$ was larger than 0.

## 3. Tsunami damage detection and classification by remote sensing

This section mainly focuses on how remote sensing is used for further research on the detailed classification of tsunami damage areas using structural damage as an example. By taking advantage of satellite remote sensing, the spatial distribution of structural damage by a tsunami can be identified. SAR images are widely used to determine tsunami-affected or inundated areas using the reflection property or backscattering coefficient as mentioned in the previous section. However, through inspecting a set of pre- and post-tsunami satellite images visually or manually, the presence of building roofs can be interpreted. The highest spatial resolution of commercial optical satellite imaging is up to 60-70 cm (QuickBird) or 1 m (IKONOS). The advantage of using high-resolution optical satellite images for damage interpretation is the capability of understanding structural damage visually. These images also enable us to comprehend the spatial extent of damage at the regional scale, where post-tsunami surveys hardly penetrate because of limited of survey time and resources. However, note that no structural types were identified by the interpretation of the satellite images. Additionally, the damage feature that can be identified from the satellite images is only structural destruction or major structural failure, which reveals the change of a roof's shape, namely "collapsed" and "major or severe damage." Accordingly, the interpretation "Destroyed" means "Collapsed" or "Major or severe damage," and "Survived" is classified as "Moderate," "Minor," "Slight" and "No" damage. An example of building damage classification is shown in Fig. 7.

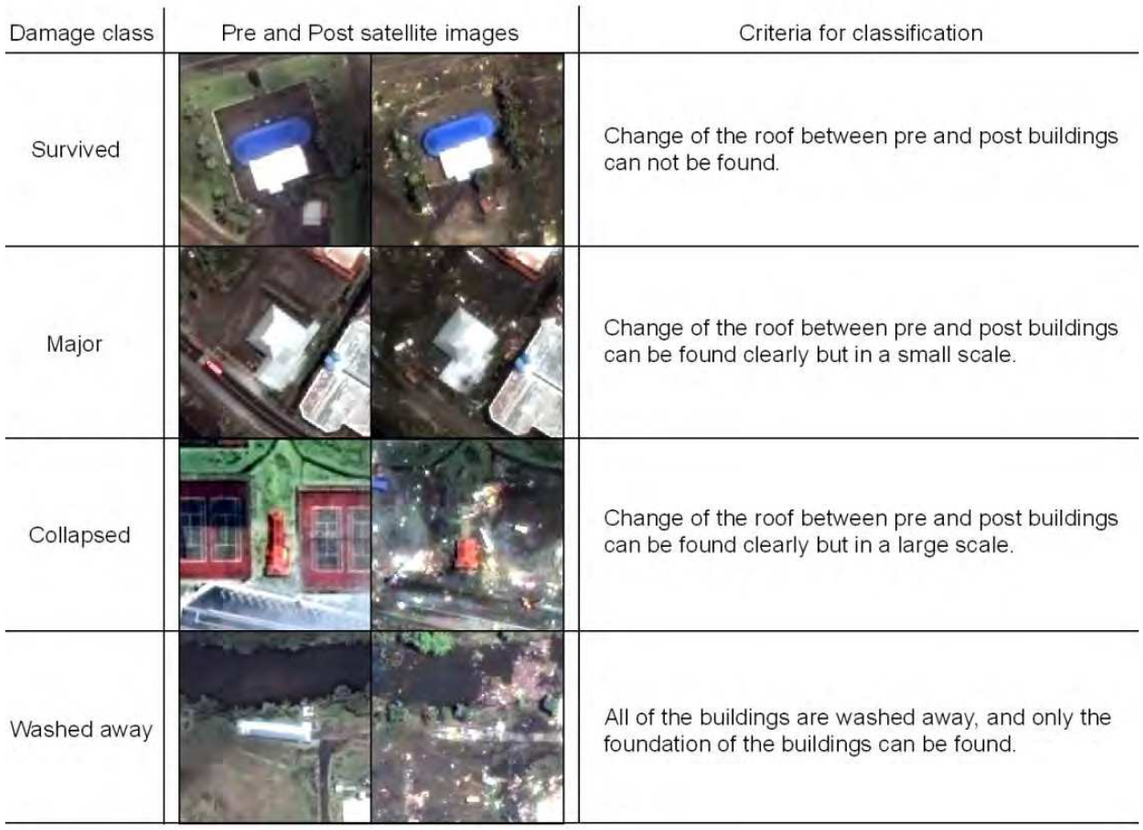


Fig. 7. Example of building damage classification criteria for the 2009 Samoa tsunami

### 3.1 The 1993 Hokkaido Nansei-Oki tsunami

In 1993, a tsunami accompanied by a M7.8 earthquake off the south–west coast of Hokkaido, Japan, struck Okushiri Island, which is 30 kilometers west of Hokkaido, within 5 minutes after the quake, causing more than 200 casualties. In particular, the Aonae district in the southernmost area of Okushiri Island suffered devastating damage due to an approximately 11-m tsunami that struck from the west coast of the island as well as fire caused during and after the tsunami attack (Murosaki, 1994). Visual damage inspection was conducted using pre- and post–tsunami aerial photographs acquired on 29 October 1990 and 14 July 1993 (one day after the event occurred), as shown in Fig. 8. Because the Aonae district suffered from extensive fire during and after the tsunami attack, it is not possible to discriminate between tsunami and fire damage by the aerial photographs alone. Thus, focusing on the existence of house roofs, the structural damage was categorised into five classes according to the damage area, whether flooded or burned, reported by Shuto (2007). The number of inspected houses and structures was 769, and the result of the structural damage interpretation in Aonae district is shown in Table 1 (Koshimura et al., 2009a). The method to detect the damaged area using SAR image analysis was applied to the tsunami-affected area in Okushri Island. Using a set of pre- and post–tsunami SAR images acquired by JERS (Japanese Earth Resources Satellite), Matsuoka & Yamazaki (2002) calculated the correlation and difference in the backscattering coefficient to represent the changes in the tsunami-affected area. To detect the impacted area, the discriminant score, Equation (2), was

| Damage category | Cause | Number of houses |
|---|---|---|
| Destroyed or Major damage | Flooded by tsunami | 417 |
| Destroyed, Burned or Major damage | Flooded by tsunami and burned by fire | 123 |
| Burned or Major damage | Burned by fire | 75 |
| Destroyed | Unknown | 11 |
| Survived (Moderate, slight or no damage) | – | 143 |

Table 1. Results of structural damage interpretation in Aonae district, Okushiri Island

incorporated, and the values of parameters A and B were modified to 1.277 and 2.729, respectively. Fig. 8 shows a comparison among the results of the visual damage interpretation of the aerial photographs, the post–tsunami JERS/SAR image (Fig. 8(b)) and the discriminant score $Z_{R1}$ (or $Z_{Rj}$). It is found that $Z_{R1}$ represents relatively larger values in severely impacted areas and that $Z_{R1}$ (Fig. 8(c)) is likely to be fairly consistent with the results of the visual interpretation (Fig. 8(a)). To increase the capability of the SAR image analysis to detect the tsunami impacted area, further discussion is required to explore the relationships between $Z_{R1}$ and the structural damage probability by correlating both with regard to the JERS/SAR resolution.

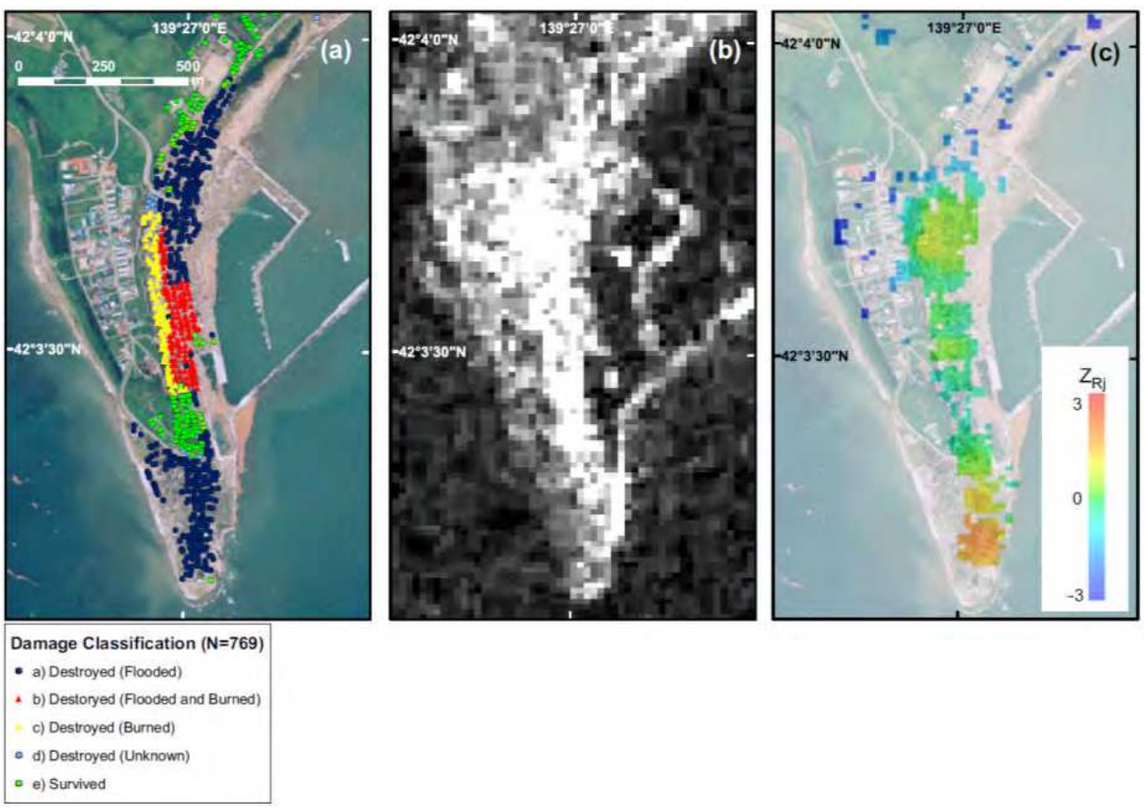


Fig. 8. Comparison among (a) the result of the visual damage interpretation of the aerial photographs, (b) the post–tsunami JERS/SAR image and (c) the discriminant score $Z_{R1}$

### 3.2 The 2004 Indian Ocean tsunami

The 2004 Indian Ocean megathrust earthquake occurred on 26 December 2004, creating a gigantic tsunami striking coastal communities over a large area. The earthquake, with a magnitude of 9.3 was the second largest ever recorded and caused the deadliest tsunami disaster in history. The tsunami devastated 11 Asian and African countries, and at least 282,517 people lost their lives. There were two locations to which satellite images were applied for tsunami damage detection, Indonesia and Thailand.

#### 3.2.1 Banda Aceh, Indonesia

Banda Aceh, a city in northern Sumatra, Indonesia, suffered more than 70,000 casualties and 12,000 house damage incidents during the 2004 event. We acquired the post–tsunami survey data from JICA (2005), which was based on a visual interpretation of the pre- and post–tsunami satellite imageries (IKONOS) with some random field checks, focusing on the existence of the individual structures' roofs. Figure 16 indicates the post–tsunami survey result in terms of structural damage in the city by JICA (2005). As shown in the right panels of the figure, the use of high–resolution optical satellite images has the capability to detect individual damages and be utilised as a promising technology for post–disaster damage investigation. Throughout the visual inspection of the two satellite images, the remaining roofs were interpreted as "Survived" and the roofs that disappeared as "Destroyed". The total number of inspected buildings in the tsunami-inundated area was 48,910, of which 16,474 were interpreted as destroyed and 32,436 as survived, as shown in Fig. 9 (Koshimura et al., 2009c).

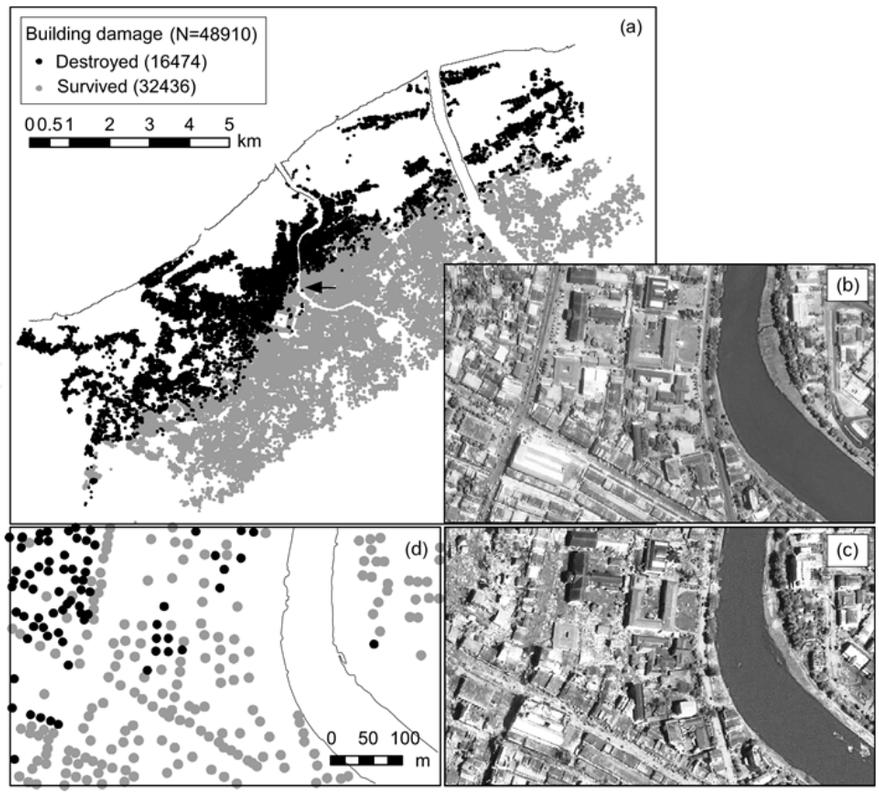


Fig. 9. Visual damage inspection results in Banda Aceh, Indonesia

### 3.2.2 Phang Nga and Phuket, Thailand

Phang Nga and Phuket were two of six southern Andaman coast provinces that were damaged by the tsunami. They provinces are famous for sightseeing areas such as Khao Lak and Patong. Therefore, reinforced concrete (RC) buildings are common in this area. Regarding structural damage, 4,806 houses were affected by the tsunami, of which 3,302 houses were destroyed completely, and as many as 1,504 were partly damaged. The maximum water level of approximately 15 m reported at Khao Lak in the Phang Nga province and of 7 m at Kamala and Patong Beach in Phuket gave these areas their respective distinction as the worst and second-worst areas, with structural damage to 2,508 and 1,033 houses, respectively. High-resolution satellite images (IKONOS) taken before and after the tsunami event were used for visual damage interpretation. The pre-event images were acquired on 13 January 2003 and 24 January 2004 for Phang Nga and Phuket; the post-event images were both acquired on 15 January 2005. In a recent study (Gokon et al., 2011), four damage levels were classified "Not collapsed" (moderate, slight or no damage), "Major damage", "Collapsed" and "Washed away," using a QuickBird satellite image with a 0.6×0.6 $m^2$ resolution. However, the 1.0×1.0 $m^2$ resolution of the IKONOS satellite image is not fine enough for a visual interpretation to differentiate the damage levels of buildings. Therefore, the classification of the building damage in this study was limited to "Not destroyed" and "Destroyed" (Koshimura et al., 2009c). The remaining roof buildings were interpreted as "Not destroyed" and those that had disappeared were classified as "Destroyed". Note that the buildings classified as "Not destroyed" may have had some sort of Damage that could be identified by the satellite images. The results of the building damage inspection in residential areas are presented in Fig. 10 (Suppasri et al., 2011a), which shows damaged buildings in residential areas in Khao Lak, Phang Nga province (1,722 destroyed and 1,285 not destroyed) and the populated residential areas in Kamala and Patong, Phuket province (233 destroyed and 1,356 not destroyed). The visual interpretation data resulted in an accuracy of more than 90 per cent after being checked with the investigation data.


Fig. 10. Visual damage inspection results in Phang Nga and Phuket, Thailand

### 3.3 The 2007 Solomon Islands tsunami

The 2007 Solomon Islands earthquake took place on 1 April 2007 near the provincial capital of Ghizo on Ghizo Island, in the Solomon Islands. The magnitude of this earthquake was calculated by the United States Geological Survey (USGS) as 8.1 on the moment magnitude scale. The tsunami that followed the earthquake killed 52 people. The structural/house damage was focused on Ghizo Island and was caused by the tsunami. First, the QuickBird pan-sharpened composite images of Ghizo Island were acquired pre- and post-tsunami (23 September 2003 and 5 April 2007) to build house inventories for visual damage inspection, as shown in Fig. 11 (Koshimura et al., 2010). The extent of the tsunami inundation zone is determined by the supervised classification based on the NDVI of the post-tsunami satellite imagery (Fig. 12), as already shown in section 2.1.


Fig. 11. The structural damage interpretation is divided into four classes: slight/no damage, substantial damage, collapsed and washed away

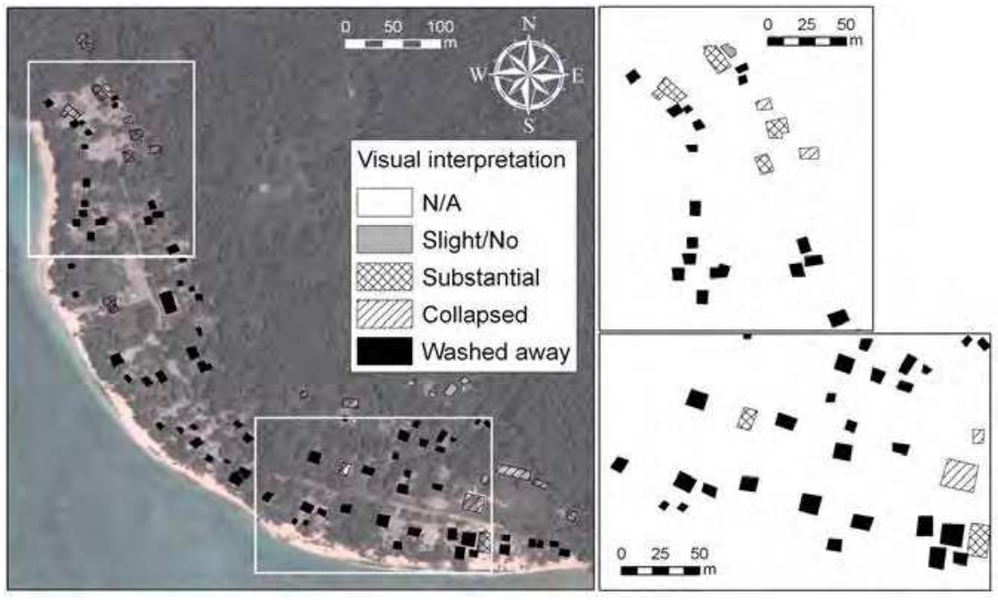


Fig. 12. Visual damage inspection results for Ghizo Island, Solomon Islands

### 3.4 The 2009 Samoa Islands tsunami

In 2009, a tsunami accompanied by a M8.1 earthquake off the southwest coast of Tutuila Island, American Samoa, struck the Samoa and Tonga islands and caused a total of 184 deaths and 7 missing. A visual damage inspection was conducted using pre- and post-tsunami QuickBird images acquired on 15 April 2007, 24 September 2009, 29 September 2009, 02 October 2009 and November 2009. The damaged structures were classified into four categories: washed-away, collapsed, major damage and survived (as previously mentioned in Fig. 7). The number of inspected houses and structures in the four study areas, namely, Pago Pago, Amanave, Poloa and Leone, totalled 451, and the results are summarised in Fig. 13 and Table 2 (Gokon et al., 2011).

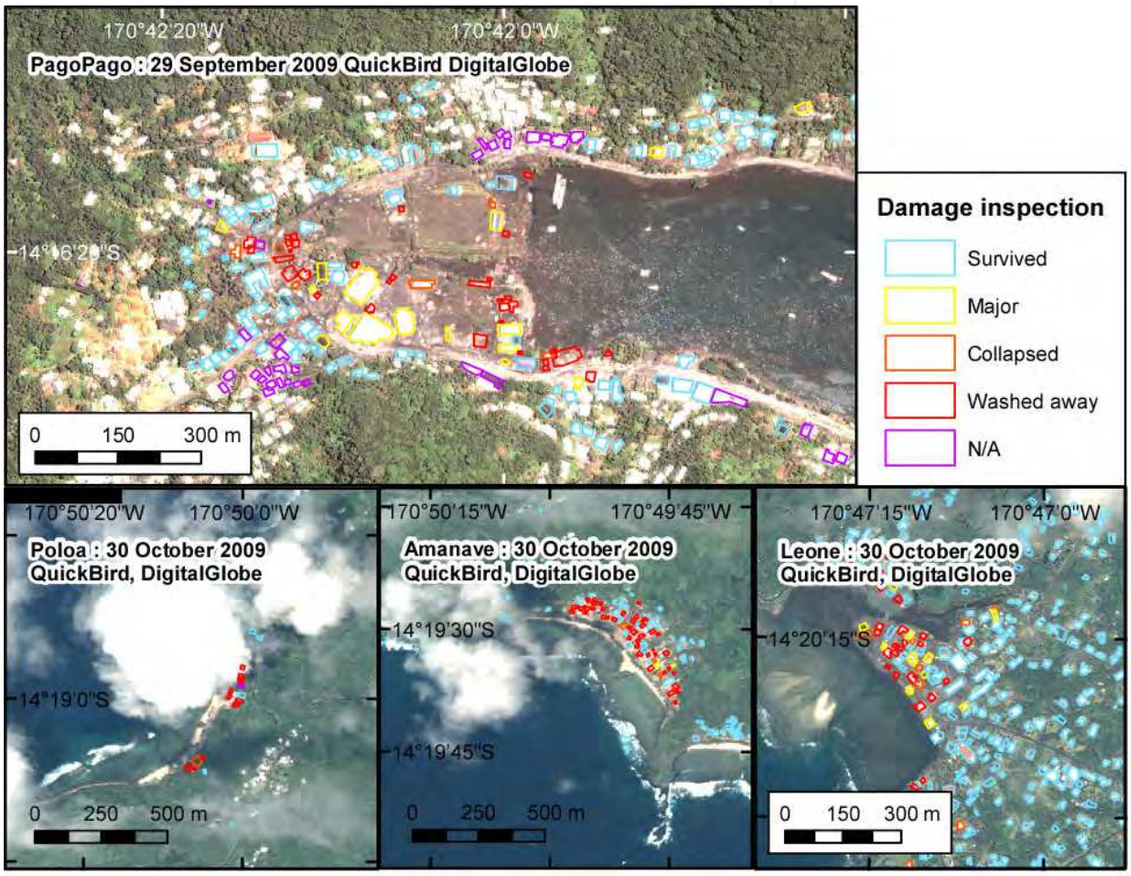


Fig. 13. Visual damage inspection results in Tutuila Island, American Samoa

| Damage category | Number of houses (Pago Pago/Amanave/Poloa/Leone/Total |
|---|---|
| Washed-away | 34/42/13/28/117 |
| Collapsed | 7/3/1/7/18 |
| Major damage | 142/0/12/28 |
| Survived | 5434/4/196/288 |

Table 2. Results of structural damage interpretation in Tutuila Island, American Samoa

### 3.5 The 2010 Chile tsunami

A moment magnitude 8.8 earthquake struck the central region of Chile on February 27, 2010. The earthquake produced a tsunami that caused major damage in locations spanning over 500 km of coastline, from Tirúa to Pichilemu. The coastal locations were affected by both ground shaking and the tsunami. As of May 2010, 521 people had died and 56 persons were still missing. The earthquake and tsunami destroyed over 81,000 houses, and another 109,000 were severely damaged. Following Matsuoka & Nojima (2009), the regression discriminant function for building damage was calculated from two characteristic values: the correlation coefficient and the difference in the backscattering coefficient for pre- and post-event SAR images (Matsuoka & Koshimura, 2010). First, following the accurate positioning of the two SAR images, a speckle noise filter with a 21×21 pixel window was applied to each image. The difference value, $d$, is calculated by subtracting the average value of the backscattering coefficient within a 13×13 pixel window in the pre-event image from the post-event image (after – before). The correlation coefficient, $r$, is also calculated from the same 13×13 pixel window. The result of applying regression discriminant analysis, using the $d$ and $r$ from the building damage dataset of the 1995 Kobe earthquake, is shown in Equation (2), where the values of parameters A and B are modified to 1.277 and 2.729, respectively. Here, $Z_{R1}$ in Equation (2) represents the discriminant score from the SAR images. The pixels whose $Z_{R1}$ value is positive are interpreted as suffering severe damage. Because both coefficients are negative, higher and negative $d$ or smaller $r$ produce larger $Z_{R1}$ values. However, in the tsunami damage areas in the PALSAR images in the abovementioned examination, the backscattered echoes were stronger in the post-tsunami image. To detect such damaged areas using image analysis, cases where the reverse occurs need to be considered. Therefore, the absolute value of the difference in the backscattering coefficient, $|d|$, was calculated, which changed the coefficient of the difference to positive values, as shown in Equation (3), where the values of parameters A and B are modified to 1.277 and 2.729, respectively. Here, $Z_{R2}$ represents the modified discriminant score. Using this formula, the pixels whose $Z_{R2}$ value is positive might be assigned as areas damaged not only by earthquakes but also by tsunamis. Using the procedure described above and the PALSAR images of the 2010 Chile earthquake tsunami, discriminant scores $Z_{R2}$ were calculated in the areas shown to be vulnerable on the inundation susceptibility maps, and the tsunami damage distribution was estimated.


Fig. 14(a). Distribution of $Z_{R2}$ obtained by ALSAR images in Talcahuano and optical images

The results are shown in Fig. 14 (a) and (b). The sections on the sea are masked, but the areas where the river could not be masked have large $Z_{R2}$ values because of the surface changes caused by the flow of water. The wetlands near Talcahuano and Llico, where the $Z_{R2}$ values are large, seem to be affected by the tsunami. Figure 14(b) shows a close-up $Z_{R2}$ image of the Dichato area, with a comparison pre- and post-tsunami from an optical image (Koshimura et al., 2011).

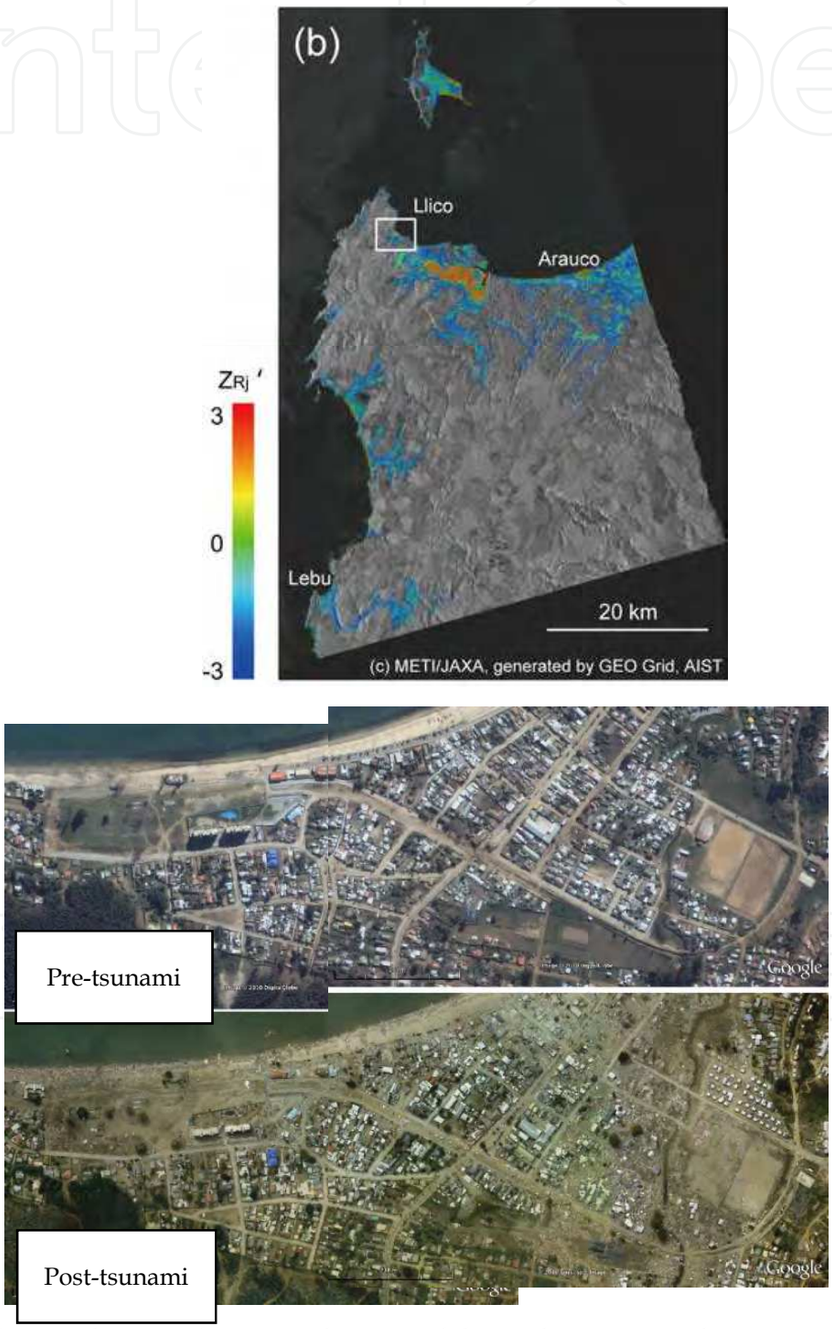


Fig. 14(b). Distribution of $Z_{R2}$ in a close-up of the Dichato area and comparison of optical images pre- and post-tsunami

### 3.6 The 2011 Tohoku tsunami

On March 11, 2011, a giant earthquake of M9.0, whose epicentre was located off the eastern part of Miyagi prefecture, Japan, caused catastrophic damage to the coastal area facing the Pacific Ocean of the Tohoku district. This earthquake caused an enormous tsunami with a run-up height that reached 40 m and destroyed approximately 270,000 houses. Aerial photos that were captured on March 12, 13 and 19 and April 1 and 5 in 2011 by GSI were used to classify the electronic building map into 2 classes: washed-away or surviving (Gokon & Koshimura, 2011). First, the panels of ortho photos, with a resolution of 80 cm/pixel, are combined with mosaic image processing. Then the electronic map and the aerial photos were integrated into the same coordinate system in ArcGIS. Finally, a visual inspection was performed for the building damage one by one (washed-away or surviving) for all the buildings in the inundation area in Miyagi prefecture, Japan. Housing damage characteristics can be explained by bathymetry conditions as follows: the Ria coast, i.e., the towns of Minami-Sanriku in Fig. 15 (upper-left), has the potential to amplify the tsunami height. As a result, the probabilities of the washed away houses in the inundation area are estimated to be over 70%. In Ishinomaki city, the number of washed away houses is small in an area located behind the breakwaters and control forests. The effect of the breakwaters and control forests in reducing tsunami damage is shown in Fig. 15 (lower-left). Most of the buildings in Matsushima town and Shiogama city, located in a bay with a small opening and almost 270 small Islands acted as natural barrier, survived the tsunami, as shown in Fig. 15 (right).

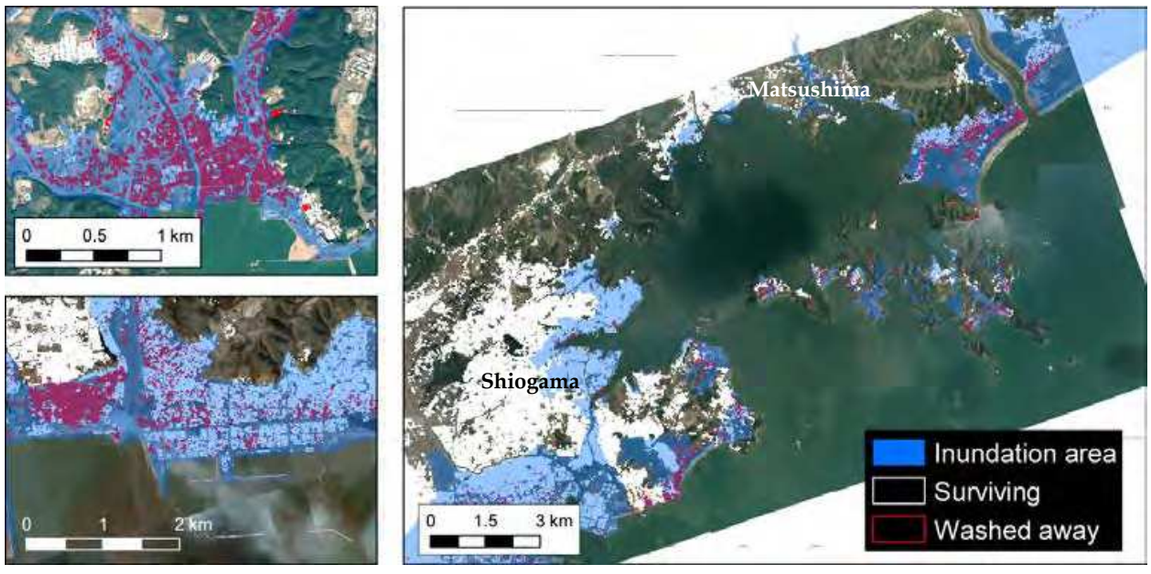


Fig. 15. Visual damage inspection results in Minami-Sanriku town (upper-left), Ishinomaki city (lower-left), and Matsushima town and Shiogama city (right). The red rectangles show washed away houses and the blue areas indicate tsunami inundation areas.

## 4. Developing a tsunami vulnerability function by applying a numerical model

The next step is to apply the previous damage inspection data with the tsunami numerical model. One method is to develop a fragility curve (Koshimura et al., 2009b). The tsunami

fragility curve is a function used to estimate the structural fragility against tsunami hazards. Visual inspections of satellite images taken before and after tsunami events are to be used to classify whether the buildings were destroyed or not based on the remaining roofs. Then a tsunami inundation model is created to reconstruct the tsunami features, such as inundation depth, current velocity, and hydrodynamic force of the event. For the tsunami inundation model, a set of nonlinear shallow water equations are discretised using the Staggered Leap-frog finite difference scheme (Imamura, 1995), with the bottom friction in the form of Manning's formula according to a land use condition. In general, two methods exist for modelling flow resistance depending on the relation between the scale of an obstacle and the grid size: the topography model and the equivalent roughness model. The topography model is used when the grid size is finer than the obstacle. The tsunami in the model simulation will not pass into a grid space that is occupied by an obstacle. Then the flow around an obstacle and the contracting flow between obstacles can be simulated. However, in a larger grid size, such as that of this study, the obstacle is smaller than the grid size. The equivalent roughness model is then appropriate for this problem. In a non-residential area, the roughness coefficient is inferred from land use, and it is used to quantify the Manning's roughness coefficient ($s \cdot m^{-1/3}$). The lowest Manning's roughness coefficient is 0.02 for smooth ground, followed by 0.025 for shallow water or natural beach and by 0.03 for vegetated area. However, Manning's roughness coefficient in a densely populated area is highly affected by the number of buildings in each computational grid. In a densely populated town, in which the building occupation ratio is high, the resistance law with the composite equivalent roughness coefficient according to land use and building conditions was first studied by Aburaya & Imamura (2002), as shown in Equation (4).

$$n = \sqrt{n_0^2 + \frac{C_D}{2gw} \times \frac{\theta}{100 - \theta} \times D^{4/3}} \tag{4}$$

In this equation, $n_0$ signifies the Manning's roughness coefficient ($n_0$=0.025, $s \cdot m^{-1/3}$), $\theta$ denotes the building/house occupation ratio in percentage varying within the range from 0 to 100 in the finest computational grid of 52 m and obtained by calculating the building area over the grid area using GIS data. $C_D$ represents the drag coefficient ($C_D$=1.5), $w$ stands for the horizontal scale of houses, and $D$ is the modelled flow depth. Fragility curves can be developed for various types, such as building material (wood, block or reinforced concrete), number of floors and country. Developed tsunami fragility curves are crucial for future tsunami risk assessment when tsunami hazards and exposure data are given.

### 4.1 Method and procedure for developing tsunami fragility curves

To develop tsunami fragility curves, a statistical approach is used with a synergistic use of the numerical model results and damage data by the procedure itemised below.

*Damage data acquisition*

The damage data was obtained from pre- and post–tsunami aerial photographs (e.g., number of destroyed or surviving structures).

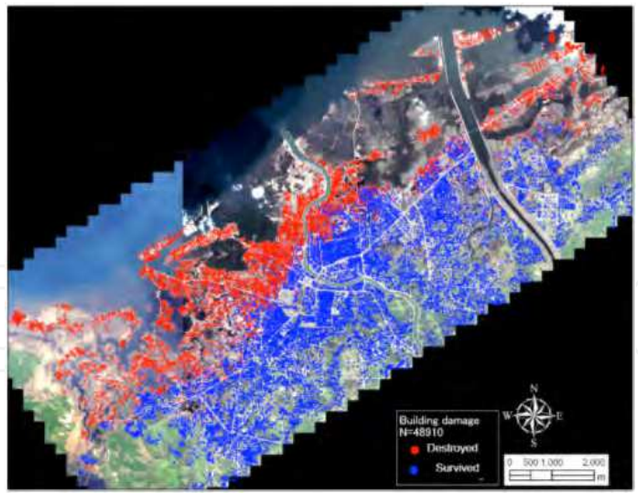


Fig. 16. Tsunami damage detected by the visual interpretation of IKONOS pre- and post-tsunami imageries. The red dots indicate totally damaged houses and the blue dots not-damaged.

*Tsunami hazard estimation*

Speculate the hydrodynamic feature of tsunamis by numerical modelling.

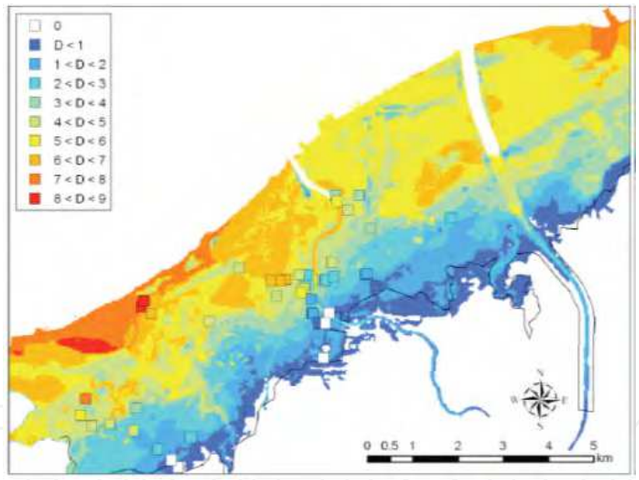


Fig. 17. Modelled tsunami inundation in the city of Banda Aceh. The result is validated by the measured flow depth shown with the squares in the figure.

*Data assimilation between the damage data and tsunami hazard information*

Correlate the damage data and the hydrodynamic features of tsunami inundation through the GIS analysis.

*Sample determination*

Sample sorting by the level of hydrodynamic features to explore an arbitrary range of these features such that each range includes the determined number of samples; check the data distribution.

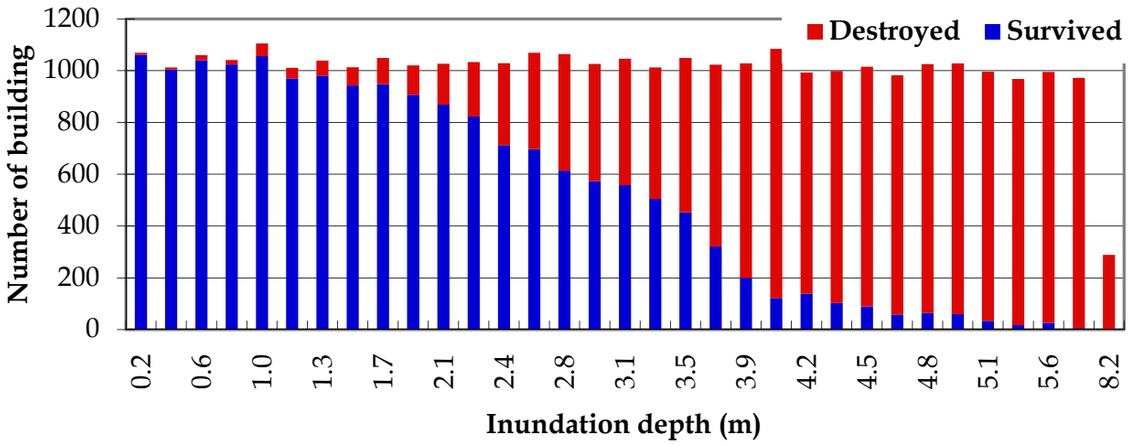


Fig. 18. Histogram of damaged and not-damaged houses to calculate the damage probability

*Calculating damage probability*

Calculate the structural damage probabilities by counting the number of destroyed or surviving structures within each range of the tsunami hydrodynamic features described above.

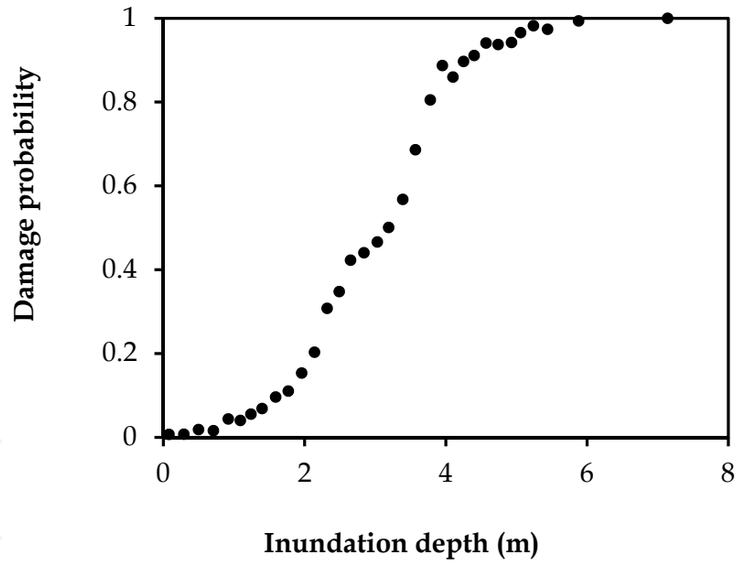


Fig. 19. The plot of damage probabilities and the median values of inundation depths that were compiled from sample data

*Regression analysis*

Determine the fragility curves by the regression analysis of the discrete set of the structural damage probabilities and hydrodynamic features of a tsunami. The damage probabilities of buildings and a discrete set were calculated and shown against a median value within a range. Linear regression analysis was performed to develop the fragility function.

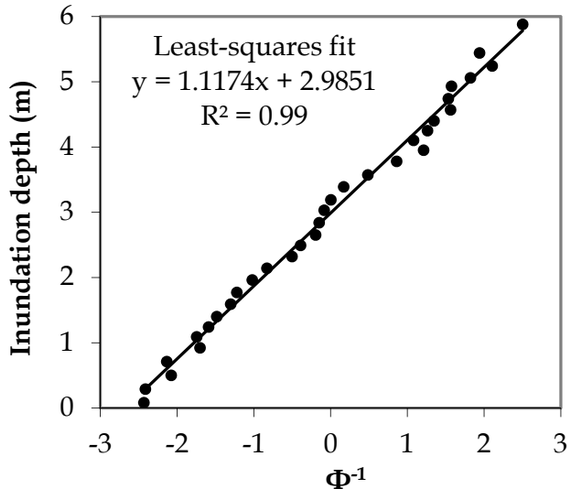


Fig. 20. An example of the plot on normal probability paper

Taking as an analogy earthquake engineering studies, the cumulative probability *PD* of damage occurrence is assumed to be given with two statistical parameters, ($\mu$, $\sigma$) or ($\mu'$, $\sigma'$). The cumulative probability *P* of the occurrence of damage is given either by Equation (5) or (6):

$$P(x) = \Phi\left[\frac{x-\mu}{\sigma}\right] \tag{5}$$

$$P(x) = \Phi\left[\frac{\ln x-\mu'}{\sigma'}\right] \tag{6}$$

In these equations, $\Phi$ represents the standardised normal (log-normal) distribution function, $x$ stands for the hydrodynamic feature of the tsunami (e.g., inundation depth, current velocity and hydrodynamic force), and $\mu$ and $\sigma$ ($\mu'$ and $\sigma'$), respectively, signify the mean and standard deviation of $x$ (ln $x$). Two statistical parameters of the fragility function, $\mu$ and $\sigma$ ($\mu'$ and $\sigma'$), are obtained by plotting $x$ (ln $x$) against the inverse of $\Phi$ on normal or log-normal probability papers and performing a least-squares fitting of this plot. Consequently, two parameters are obtained by taking the intercept (= $\mu$ or $\mu'$) and the angular coefficient (= $\sigma$ or $\sigma'$) in Equations (7) or (8):

$$x = \sigma\Phi^{-1} + \mu \tag{7}$$

$$\ln x = \sigma'\Phi^{-1} + \mu' \tag{8}$$

Throughout the regression analysis, the parameters are determined as shown in Table 8 to obtain the best fit of fragility curves with respect to the inundation depth, the maximum current velocity and the hydrodynamic force on structures per unit width. Here, the hydrodynamic force acting on a structure is defined as its drag force per unit width as

$$F = \frac{1}{2}C_D\rho u^2 D \tag{9}$$

where $C_D$ denotes the drag coefficient ($C_D$ = 1.0 for simplicity), $\rho$ is the density of water (= 1,000 kg/m$^3$), $u$ stands for the current velocity (m/s), and $D$ is the inundation depth (m). From this result, all the fragility functions with respect to the inundation depth, current velocity and hydrodynamic force are given by the standardised lognormal distribution functions with $\mu'$ and $\sigma'$. It should be noted that because the damage interpretation using the pre- and post–tsunami satellite images focused on whether the houses' roofs remained, we supposed that the structural damage was caused by the tsunami inundation. Additionally, note that the tsunami damage to structures was caused by both hydrodynamic force/impact and the impact of floating debris, i.e., these facts are reflected in the damage probabilities but not in the numerical model results (the estimated hydrodynamic features). In that sense, the present fragility functions might indicate overestimation in terms of the damage probabilities to the hydrodynamic features of the tsunami inundation flow.

### 4.2 Tsunami fragility curves for Okushiri Island, Japan

The task of discriminating between the damage caused by tsunami inundation or by fire was quite speculative. Thus, fragility curves were developed using 523 houses within the inundation zone estimated by the numerical model. A relationship between the damage probability and the tsunami's hydrodynamic features were obtained as a discrete set of structural damage probabilities using a range of approximately 50 buildings and the tsunami hazard. The relationship was explored with the form of a fragility curve by performing the regression analysis. Structural damage is severe when the inundation depth is greater than 3 m, the current velocity is greater than 4 m/s and the hydrodynamic force is greater than 25 kN/m (Fig. 21).

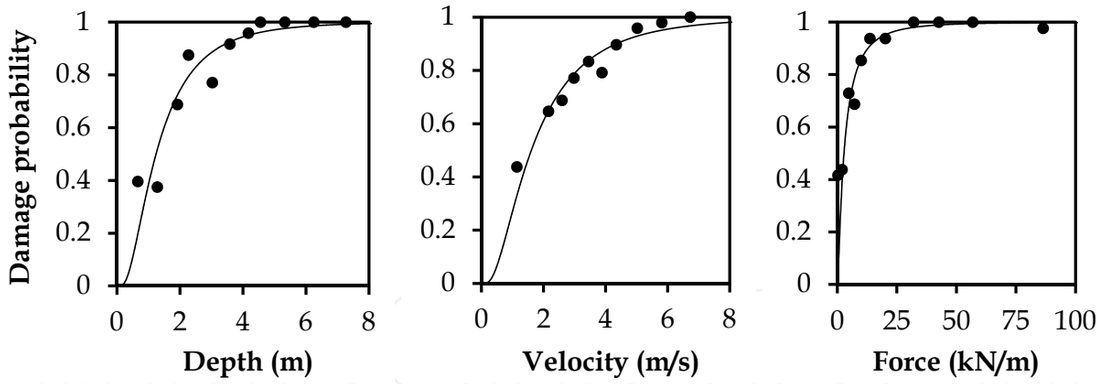


Fig. 21. Tsunami fragility curves as a function of tsunami features for Okushiri Island

### 4.3 Tsunami fragility curves for Banda Aceh, Indonesia

The number of destroyed buildings in Banda Aceh is 16,474, and the number of surviving building is 32,436 based on the remaining roofs. The damage probabilities of buildings and a discrete set were calculated and shown against a median value within a range of approximately 1,000 buildings. Linear regression analysis was performed to develop the fragility function. As a result, the fragility curves are obtained as Figure 20, indicating the damage probabilities according to the hydrodynamic features of the tsunami inundation flow in Banda Aceh. For instance, the structures were significantly vulnerable when the

local inundation depth exceeds 2 or 3 m, the current velocity exceeds 2.5 m/s or the hydrodynamic load on a structure exceeds 5 kN/m (Fig. 22).

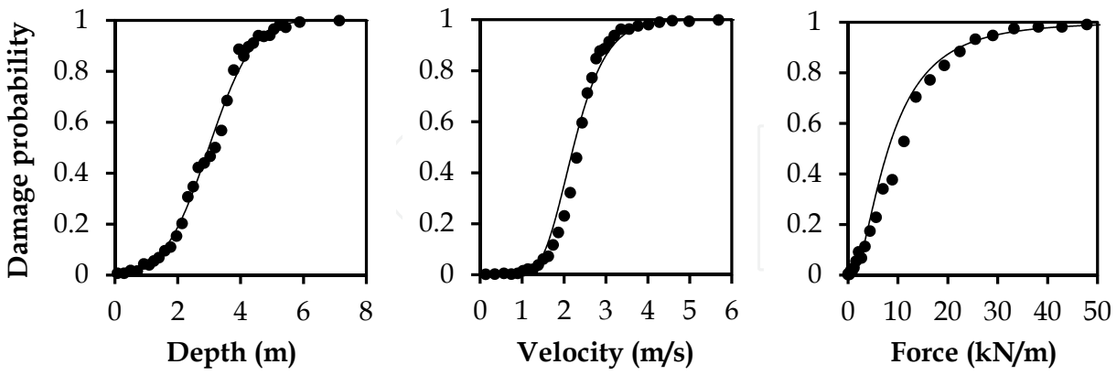


Fig. 22. Tsunami fragility curves as a function of tsunami features for Banda Aceh

### 4.4 Tsunami fragility curves for Phang Nga and Phuket, Thailand

From the visual inspection of damaged buildings based on the remaining roof structures, a histogram of tsunami features (inundation depth, current velocity, and hydrodynamic force) and the number of buildings, including those not destroyed and those destroyed, was plotted. The damage probabilities of buildings and a discrete set were calculated and shown against a median value within a range of approximately 100 buildings in Phang Nga and 50 buildings in Phuket. Linear regression analysis was performed to develop the fragility function. The differences in damage characteristics of the buildings in Phang Nga and Phuket due to the construction materials are represented by the developed fragility curves in this study (Fig. 23 (a) and (b)). Although the inundation depth of 6 m engenders 100% damage probability in both locations, a lower inundation depth of 2 m is more fragile in Phang Nga: the damage probability would be 25% in Phuket but would be as high as 35% in Phang Nga.

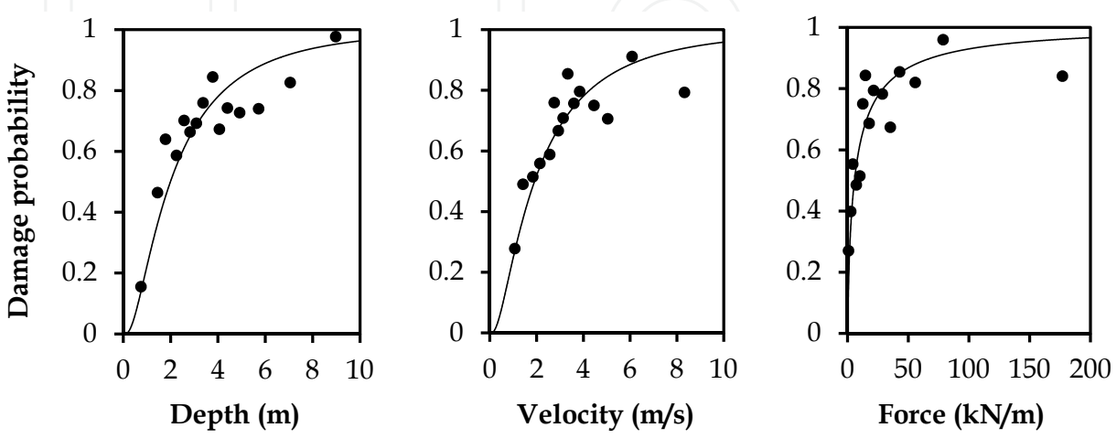


Fig. 23(a). Tsunami fragility curves as a function of tsunami features for Phang Nga

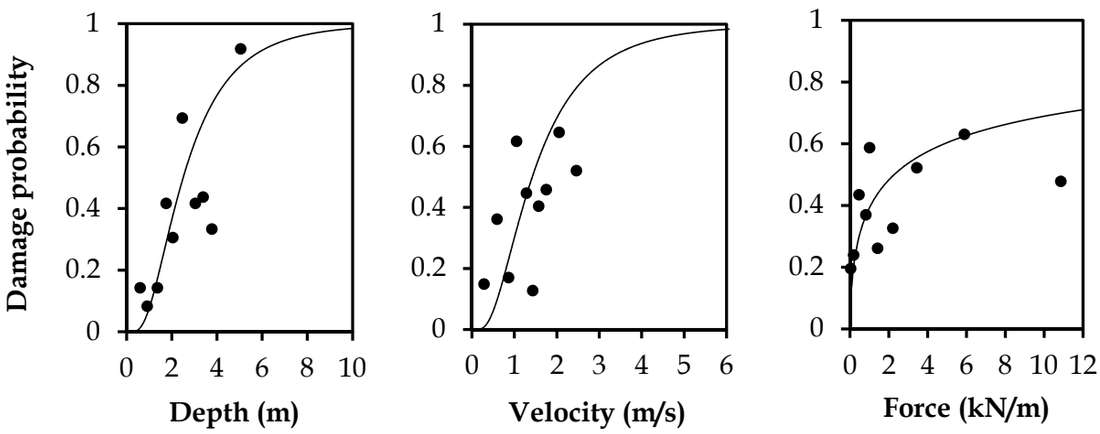


Fig. 23(b). Tsunami fragility curves as a function of tsunami features for Phuket

### 4.5 Tsunami fragility curves for American Samoa, USA

A visual inspection shows that there were 134 damaged and 210 surviving houses. The damage probabilities were calculated using a range of 20 buildings, and a linear regression analysis was performed. From Fig. 24, 80% of the buildings were damaged when the inundation depth exceeds 6 m. More than half of the buildings were damaged if the current velocity exceeds 2 m/s. The damage due to the hydrodynamic force increased rapidly up to 10 kN/m.

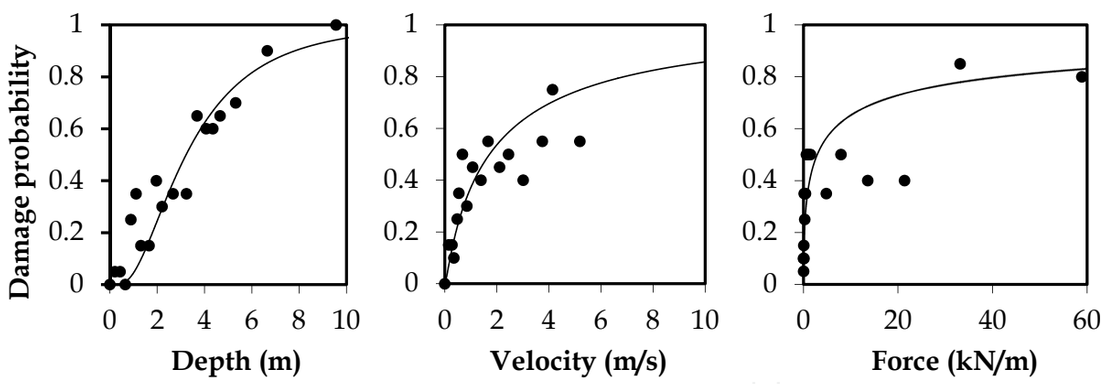


Fig. 24. Tsunami fragility curves as a function of tsunami features for American Samoa

### 4.6 Summary of statistical parameters for developed fragility curves

Tsunami fragility curves were developed using a numerical model and a visual inspection of satellite images in several countries (Japan, Indonesia, Thailand and American Samoa) with different building materials (wood or reinforced concrete). The necessary statistical parameters for plotting the fragility curves with inundation depth, current velocity and hydrodynamic force are summarised in Table 3.

| Event (Year) | Location | Tsunami feature | Building type | μ | σ | μ' | σ' | R2 |
|---|---|---|---|---|---|---|---|---|
| Nansei Hokkaido (1993) | Okushiri Island | Inundation depth | Mainly wood | | | 0.216 | 0.736 | 0.82 |
| | | Current velocity | | | | 0.475 | 0.776 | 0.89 |
| | | Hydrodynamic force | | | | 1.033 | 1.186 | 0.92 |
| Indian Ocean (2004) | Banda Aceh | Inundation depth | Mainly wood & brick | 2.985 | 1.117 | | | 0.99 |
| | | Current velocity | | | | 0.799 | 0.278 | 0.97 |
| | | Hydrodynamic force | | | | 2.090 | 0.791 | 0.99 |
| Indian Ocean (2004) | Phang Nga | Inundation depth | Some RC | | | 0.689 | 0.903 | 0.80 |
| | | Current velocity | | | | 0.649 | 0.952 | 0.72 |
| | | Hydrodynamic force | | | | 1.748 | 1.937 | 0.75 |
| | Phuket | Inundation depth | | | | 0.917 | 0.642 | 0.62 |
| | | Current velocity | | | | 0.352 | 0.675 | 0.32 |
| | | Hydrodynamic force | | | | 0.821 | 3.000 | 0.50 |
| Samoa (2009) | American Samoa | Inundation depth | Some RC | | | 1.170 | 0.691 | 0.89 |
| | | Current velocity | | | | 0.541 | 1.650 | 0.73 |
| | | Hydrodynamic force | | | | 1.070 | 3.160 | 0.72 |

Table 3. Summary of statistical parameters for developed fragility curves

## 5. Conclusion

This chapter introduced how remote sensing can be applied for tsunami research fields. In general, remote sensing is used for rapid and large-scale damage detection to understand the scale of a tsunami, especially when accessibility to disaster-affected areas is limited in the immediate aftermath. Some of the general applications shown in this chapter are related to the tsunami inundation limit, damaged buildings/debris and mangrove recovery monitoring. SAR images are used to determine tsunami-affected areas using the reflection property or backscattering coefficient as mentioned in the previous section. The next step focused on damage classification in a tsunami affected area, i.e., structural damage of housing or buildings. The benefit of high-resolution images from the sky helps tsunami researchers interpret the tsunami damage level based on roofs. A one-metre resolution, such as that of IKONOS, could help classify buildings as destroyed or not destroyed. In addition, a very high-resolution satellite image such as QuickBird (0.6 m resolution) was used to classify a number of levels, i.e., washed-away, collapsed, major damage or survived. Some recent research on tsunami events was introduced, namely, the 1993 Hokkaido Nansei-oki tsunami, the 2004 Indian Ocean tsunami, the 2007 Solomon tsunami, the 2009 Samoa tsunami, the 2010 Chile tsunami and the most recent 2011 Tohoku tsunami. However, information from the sky has some limitations because it is impossible to make a detailed damage inspection of a structural member, and it might have some errors compared with an actual field survey. Finally, classified structural damage data from a visual interpretation of high-resolution satellite images were used in combination with the tsunami numerical simulation to develop tsunami vulnerability curves called tsunami fragility curves. Tsunami

features during inundation, such as inundation depth, current velocity and hydrodynamic force can be simulated by the numerical model. The tsunami fragility function can be constructed by combining the inspected damage data and simulated tsunami features using a statistical approach. The developed tsunami fragility curves for each location could be important tools for tsunami risk assessment against potential future tsunamis. However, applying tsunami fragility for future risk evaluation should be performed with care. The structural characteristics and behaviour of housing and buildings differ by country (Fig. 24). For example, an RC-frame building with brick walls is common in Southeast Asian countries. However, wooden walls are commonly used in Japan because of their light weight for reducing damage from earthquakes. These differences cause the tsunami damage characteristics to be different (Suppasri et al., 2011b).

Fig. 25. Examples of building damage in the case of the 2004 Indian Ocean tsunami in Thailand and the 2011 Tohoku tsunami in Japan

## 6. Acknowledgment

QuickBird images are owned by DigitalGlobe, Inc. and IKONOS images are operated by GeoEye. ASTER and PALSAR images are owned by METI/NASA and METI/JAXA, respectively, and both are processed by GEO Grid, AIST. JERS-1/SAR image is also owned by METI/JAXA. TerraSAR-X image is the property of Infoterra GmbH and distributed by PASCO Corporation. We express our deep appreciation to the Industrial Technology Research Grant Program in 2008 (Project ID: 08E52010a) from the New Energy and Industrial Technology Development Organization (NEDO), the Willis Research Network (WRN) under the Pan-Asian/Oceanian tsunami risk modelling and mapping project and the Ministry of Education, Culture, Sports, Science and Technology (MEXT) for the financial support for this study.

## 7. References

Aburaya, T. & Imamura, F. (2002). The proposal of a tsunami run–up simulation using combined equivalent roughness, *Proceedings of the Coastal Engineering Conference (JSCE)*, 49, 276–280 (in Japanese)

Gokon, H. & Koshimura, S. (2011). Mapping of buildings damage of the 2011 Tohoku earthquake tsunami, *Proceedings of the 8th International Workshop on Remote Sensing for Post Disaster Response*, Standford University, California, United States, 15-16 September 2011

Gokon, H.; Koshimura, S.; Matsuoka, M. & Namegaya, Y. (2011). Developing tsunami fragility curves due to the 2009 tsunami disaster in American Samoain, *Proceedings of the Coastal Engineering Conference (JSCE)*, Morioka, 9-11 November 2011 (in Japanese)

Henderson, F. M. & Lewis, A. J. (1998). Principles and applications of imaging radar, Manual of Remote Sensing, 2, John Wiley & Sons, Inc., New York

Imamura, F. (1995). Review of tsunami simulation with a finite difference method, Long-Wave Runup Models, *World Scientific*, 25–42

Kamthonkiat, D.; Rodfai, C.; Saiwanrungkul. A.; Koshimura, S. & Matsuoka, M. (2011). Geoinformatics in mangrove monitoring: damage and recovery after the 2004 Indian Ocean tsunami in Phang Nga, Thailand, *Natural Hazards and Earth System Sciences*, 11, 1851–1862

Koshimura, S.; Matsuoka, M. & Kayaba, S. (2009a). Tsunami hazard and structural damage inferred from the numerical model, aerial photos and SAR imageries, *Proceedings of the 7th International Workshop on Remote Sensing for Post Disaster Response*, University of Texas, Texas, United States, 22−23 October 2009

Koshimura, S.; Namegaya, Y. & Yanagisawa, H. (2009b). Tsunami fragility – A new measure to assess tsunami damage, *Journal of Disaster Research*, 4, 479−488

Koshimura, S.; Oie, T.; Yanagisawa, H. & Imamura, F. (2009c). Developing fragility curves for tsunami damage estimation using numerical model and post-tsunami data from Banda Aceh, Indonesia, *Coastal Engineering Journal*, 51, 243−273

Koshimura, S.; Kayaba, S. and Matsuoka, M. (2010). Integrated approach to assess the impact of tsunami disaster, *Safety, Reliability and Risk of Structures, Infrastructures and Engineering Systems*,, Taylor & Francis Group, London, pp. 2302 – 2307, ISBN 978-0-415-47557-0

Koshimura, S. & Matsuoka, M. (2010). Detecting tsunami affected area using satellite SAR imagery, *Journal of Japan Society of Civil Engineers*, Ser. B2 (Coastal Engineering), 66(1), 1426–1430 (in Japanese with English abstract)

Koshimura, S.; Matsuoka, M.; Matsuyama, M.; Yoshii, T.; Mas, E.; Jimenez, C; & Yamazaki, F. (2011). Field survey of the 2010 tsunami in Chile, *Proceedings of the 8th International Conference on Urban Earthquake Engineering,* Tokyo Institute of Technology, Japan, 7−8 March 2011

Lee, J. S. (1980). Digital image enhancement and noise filtering by use of local statistics, IEEE Trans. Pattern Analysis and Machine Intelligence, 2, 165-168

Massonnet, D.; Rossi, M.; Carmona, C.; Adragna, F.; Peltzer, G.; Fiegl, K.; & Rabaute, T. (1993). The displacement field of the Landars earthquake mapped by radar interferometry, *Nature*, 364, pp.138-142

Matsuoka, M. & Nojima, N. (2009). Estimation of building damage ratio due to earthquakes using satellite L-band SAR imagery, *Proceedings of the 7th International Workshop on Remote Sensing and Disaster Response*, University of Texas, Texas, United States, 22−23 October 2009

Matsuoka, M. & Yamazaki, F. (2002). Application of a methodology for detecting building damage area to recent earthquakes using satellite SAR intensity imageries and its validation, *Journal of Structural and Construction Engineering*, Vol. 558, pp.139–147 (in Japanese)

Matsuoka, M. & Yamazaki, F. (2004). Use of satellite SAR intensity imagery for detecting building areas damaged due to earthquakes, *Earthquake Spectra*, Vol. 20, No. 3, pp.975–994

Matsuoka, M. & Koshimura, S. (2010). Tsunami damage area estimation for the 2010 Maule, Chile earthquake using ASTER DEM and PALSAR images with the GEO grid system, *Proceedings of the 8th International Workshop on Remote Sensing for Post Disaster Response*, Tokyo Institute of Technology, Tokyo, Japan, 31 October - 1 November 2010

Murosaki, Y. (1994). Great fire in Okushiri in case of the 1993 Hokkaido Nansei–Oki earthquake, in Survey and Research on the 1993 Hokkaido Nansei–Oki Earthquake, Tsunami and Damages, Report No. 05306012, pp.161–170 (in Japanese)

Nojima, N.; Matsuoka, M.; Sugito, M. & Esaki, K. (2006). Quantitative estimation of building damage based on data integratoin of seismic intensities and satellite SAR imagery, *Journal of Structural Mechanics and Earthquake Engineering*, Japan Society of Civil Engineers, 62(4), 808–821 (in Japanese with English abstract)

Shuto, N. (2007). Damage and Reconstruction at Okushiri Town Caused by the 1993 Hokkaido Nansei–oki Earthquake Tsunami, *Journal of Disaster Research*, Vol. 2, No.1, pp.44–49

Suppasri, A.; Koshimura, S. & Imamura, F. (2011a). Developing tsunami fragility curves based on the satellite remote sensing and the numerical modeling of the 2004 Indian Ocean tsunami in Thailand, *Natural Hazards and Earth System Sciences*, 11, 173–189

Suppasri, A.; Koshimura, S. & Imamura, F. (2011b). Tsunami risk assessment for building using numerical model and fragility curves, *Proceedings of the Coastal Engineering Conference (JSCE)*, Morioka, International session, 9-11 November 2011

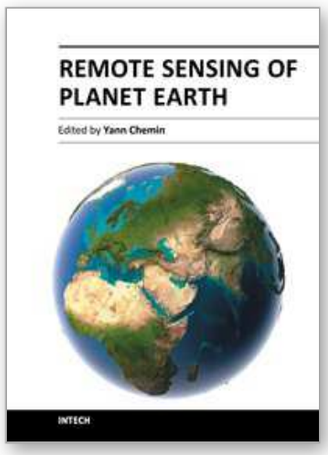


**Remote Sensing of Planet Earth**

Edited by Dr Yann Chemin

ISBN 978-953-307-919-6
Hard cover, 240 pages
**Publisher** InTech
**Published online** 27, January, 2012
**Published in print edition** January, 2012

Monitoring of water and land objects enters a revolutionary age with the rise of ubiquitous remote sensing and public access. Earth monitoring satellites permit detailed, descriptive, quantitative, holistic, standardized, global evaluation of the state of the Earth skin in a manner that our actual Earthen civilization has never been able to before. The water monitoring topics covered in this book include the remote sensing of open water bodies, wetlands and small lakes, snow depth and underwater seagrass, along with a variety of remote sensing techniques, platforms, and sensors. The Earth monitoring topics include geomorphology, land cover in arid climate, and disaster assessment after a tsunami. Finally, advanced topics of remote sensing covers atmosphere analysis with GNSS signals, earthquake visual monitoring, and fundamental analyses of laser reflectometry in the atmosphere medium.



**InTech Europe**
University Campus STeP Ri
Slavka Krautzeka 83/A
51000 Rijeka, Croatia
Phone: +385 (51) 770 447
Fax: +385 (51) 686 166
www.intechopen.com

**InTech China**
Unit 405, Office Block, Hotel Equatorial Shanghai
No.65, Yan An Road (West), Shanghai, 200040, China
中国上海市延安西路65号上海国际贵都大饭店办公楼405单元
Phone: +86-21-62489820
Fax: +86-21-62489821

IntechOpen